ly. The oxygen fugacity (fO_2) of the experiments was not buffered externally. However, fO_2 calculations based on biotite-sanidine-magnetite-H_2O-O_2 equilibrium [D. R. Wones, *Kozan Chishitsu* **31**, 191 (1981)] yield fO_2 values 1.5 to 2 log units above the nickel–nickel oxide buffer. This is consistent with the estimated fO_2 conditions of natural epidote-bearing magmas (*6*, *16*). Quenched experimental charges were sectioned longitudinally, polished, and examined with reflected-light microscopy and backscattered electron imaging. Rim widths were measured with an optical microscope equipped with a graduated ocular lens; the rim widths reported are the average of 20 to 30 measurements. Rim width data are as follows: experiment Ep-10, t = 51.17 hours, rim width = 2.74 ± 0.9 μm; experiment Ep-12, t = 141.20 hours, rim width = 4.95 ± 0.8 μm; and experiment Ep-11, t = 378.78 hours, rim width = 8.18 ± 1.3 μm.

9. D. C. Rubie and A. J. Brearley, in *High-Temperature Metamorphism and Crustal Anatexis*, J. R. Ashworth and M. Brown, Eds. (Unwin Hyman, London, 1988), pp. 57–86. See also G. W. Fisher, *Geochim. Cosmochim. Acta* **42**, 1035 (1978).
10. D. R. Baker, *Contrib. Mineral. Petrol.* **106**, 462 (1991).
11. M. W. Schmidt [*Am. J. Sci.* **293**, 1011 (1993)] conducted four experiments on epidote-bearing tonalite from which minimum and maximum apparent diffusion coefficients can be estimated. Three experiments (r29 through r31) below the epidote low-pressure stability limit (≤450 MPa) showed no trace of epidote (maximum size, 10 μm) after 500 to 504 hours at temperatures of 680° to 700°C in addition to an initial period of ≥30 hours at 720° to 750°C. These data yield a minimum D_{app} of 5×10^{-17} m^2 s^{-1}. One experiment (r28) yielded an epidote rim of ≤4 μm at 600 MPa and 720°C for ≥30 hours, from which a maximum D_{app} of 1×10^{-16} m^2 s^{-1} can be estimated.
12. Diffusivity of cations in granitic melts varies as a function of melt structure, viscosity, and water content, all of which are interrelated (*10*). Water contents of our experiments (estimated at 7.5% H_2O from totals, Table 1) agree well with expected 450-MPa water saturation conditions [C. W. Burnham, in *Geochemistry of Hydrothermal Ore Deposits*, H. L. Barnes, Ed. (Holt, Rinehart and Winston, New York, 1967), pp. 34–76] and will yield the highest diffusivities at this pressure. For lower magma water contents, magma viscosity will be higher and diffusivities will be lower, yielding longer estimates of dissolution time. However, changes in magma viscosity as a function of water content are most striking from 0 to 2% H_2O and small above 4% H_2O, and the effects of viscosity on diffusivity at high water contents should be relatively small. Differences in diffusivity of just one order of magnitude have been documented between granitic melts with 3% H_2O and 6% H_2O (*10*), which spans the range of natural granitic melt water contents [J. D. Clemens, *Lithos* **17**, 273 (1984)], and diffusivity differences of this magnitude have little significance for the conclusions drawn here.
13. Temperatures up to 850°C are typical for granitic magmas [(*16*); J. A. Whitney and J. C. Stormer, *J. Petrol.* **26**, 726 (1985)]. For extrapolation of the 750°C D_{app} values to other temperatures, an activation energy of 131 kJ mol^{-1} was used (*10*).
14. W. Johannes, *Contrib. Mineral. Petrol.* **86**, 264 (1984).
15. B. W. Evans and J. A. Vance, *ibid.* **96**, 178 (1987); R. L. Dawes and B. W. Evans, *Geol. Soc. Am. Bull.* **103**, 1017 (1991).
16. D. A. Archibald, T. E. Krogh, R. L. Armstrong, E. Farrar, *Can. J. Earth Sci.* **21**, 567 (1984); A. D. Brandon and R. St.J. Lambert, *ibid.* **30**, 1076 (1993).
17. A. D. Brandon and R. St.J. Lambert, *J. Petrol.* **35**, 239 (1994). Only the outer margin of the batholith (zone 1 to 3 km thick) has abundant epidote (from 0.1 to 3%). The middle-zone granodiorite has only minor or no epidote (less than 0.1%). The two-mica granite, for which there is geochemical evidence that it is derived from a different crustal source, has no epidote. The latter two zones are >60% of the areal exposure. Epidote in these inner zones was either completely resorbed or was never stable in these more felsic magmas.
18. J. E. Reesor, *Geol. Surv. Can. Mem. 292* (1958).
19. Epidote from the White Creek Batholith shows textures indicative of magmatic origin. These include euhedral crystal forms where protected from reaction by biotite, and cores of allanite [see (*6*, *16*)]. Magmatic epidote in granites typically has <0.2% TiO_2 by weight (*6*, *16*, *22*), whereas secondary epidote replacing biotite has >0.6% TiO_2 (*15*). Epidote from the White Creek Batholith has <0.1% TiO_2 (Table 1). The pistacite (Ps) content of magmatic epidote (Ps = molar $[Fe^{3+} / (Fe^{3+} + Al)] \times 100$) ranges from Ps_{23} to Ps_{29} [(*6*); M. T. Naney, see (*7*)]. Secondary epidote replacing plagioclase has a lower Ps content (Ps_{0-24}), and secondary epidote replacing biotite has a higher Ps content (Ps_{36-48}) [A. J. Tulloch, *Contrib. Mineral. Petrol.* **69**, 105 (1979)]. Epidote from the White Creek Batholith (Ps_{26-29}) overlaps the magmatic range (Table 1).
20. Epidote-bearing granodiorites from the White Creek Batholith have mineral assemblages appropriate for use of the Al-hornblende geobarometer [J. M. Hammarstrom and E-an Zen, *Am. Mineral.* **71**, 1297 (1986)] based on recent experimental calibrations [M. C. Johnson and M. J. Rutherford, *Geology* **17**, 837 (1989) = PJR below; M. W. Schmidt (*7*) = PS below]. See Table 1 for a typical hornblende analysis. For this analysis, we obtained pressures of 240 and 360 MPa, respectively, using the PJR and PS geobarometers. For 16 hornblende analyses from samples WC-18 and WC-19, we obtained a range of 210 to 280 MPa and a mean of 240 MPa (depth of 8.4 km) using the PJR geobarometer, and a range of 320 to 400 MPa and a mean of 360 MPa (depth of 12.6 km) using the PS geobarometer.
21. H. Nekvasil, *Am. Mineral.* **73**, 966 (1988).
22. C. R. Vyhnal, H. Y. McSween, J. A. Speer, *ibid.* **76**, 176 (1991); A. J. Tulloch, *Geology* **14**, 186 (1986); R. H. Moench, *ibid.*, p. 187.
23. We thank B. Evans and R. Dawes for sample material, R. W. Luth for laboratory facilities, M. Walter for initial experiments, A. Locock for the epidote sample, P. Wagner for electron microprobe assistance, and P. Resultay for timely polishing of the charges, and R. W. Luth, J. Farquhar, D. R. M. Pattison, and three anonymous reviewers for helpful comments. Supported by Natural Sciences and Engineering Research Council of Canada research grants to R.A.C. and T.C. A.D.B. is supported by a Carnegie Institution Post-Doctoral Fellowship.

20 September 1995; accepted 16 January 1996

Enhancement of Solution NMR and MRI with Laser-Polarized Xenon

G. Navon,* Y.-Q. Song, T. Rõõm, S. Appelt, R. E. Taylor, A. Pines†

Optical pumping with laser light can be used to polarize the nuclear spins of gaseous xenon-129. When hyperpolarized xenon-129 is dissolved in liquids, a time-dependent departure of the proton spin polarization from its thermal equilibrium is observed. The variation of the magnetization is an unexpected manifestation of the nuclear Overhauser effect, a consequence of cross-relaxation between the spins of solution protons and dissolved xenon-129. Time-resolved magnetic resonance images of both nuclei in solution show that the proton magnetization is selectively perturbed in regions containing spin-polarized xenon-129. This effect could find use in nuclear magnetic resonance spectroscopy of surfaces and proteins and in magnetic resonance imaging.

Sensitivity poses a persistent challenge to nuclear magnetic resonance (NMR) spectroscopy and magnetic resonance imaging (MRI). One problem is low spin polarization, the very small population difference between "up" and "down" spins, which is usually no more than 1 in 10^5 at thermal equilibrium at room temperature. Lower temperatures and higher fields can provide only limited relief, so spectroscopists have resorted, instead, to schemes such as optical pumping and dynamic nuclear polarization in order to enhance the polarization.

Optical pumping (OP) methods (*1*) transfer angular momentum from circularly polarized light to electronic and nuclear spins. The exchange of angular momentum, often accomplished in one or more steps, reorients the spins and thus alters the polarization. After OP effects were shown for the nuclear spins of gaseous ^3He in a He/Rb mixture (*2*), the method was subsequently further developed at Princeton for ^{129}Xe as well as ^3He (*3*). The strong NMR signals obtained from hyperpolarized gases have since extended the use of high-resolution ^{129}Xe NMR and MRI (*4*), giving rise to a number of experiments, among them enhanced surface NMR of ^{129}Xe (*5*), signal enhancement of proton and ^{13}C NMR by thermal mixing (*6*, *7*), and Hartmann-Hahn cross-polarization (*8*), polarized gas gyroscopes (*9*, *10*), and, most recently, enhanced MRI of void spaces in organisms (such as the lung) and materials (*11*, *12*).

Dynamic nuclear polarization (*13*, *14*) arises from the cross-relaxation between coupled spins. When the polarization of one spin species is disturbed, the polarization of a neighboring species deviates from equilib-

Materials Sciences Division, Lawrence Berkeley National Laboratory, and Department of Chemistry, University of California, Berkeley, CA 94720, USA.

*Permanent address: School of Chemistry, Tel Aviv University, Tel Aviv 69978, Israel.
†To whom correspondence should be addressed at the Department of Chemistry, University of California, Berkeley, CA 94720, USA.

rium while the coupled system relaxes. Originally exploited to transfer polarization from electronic to nuclear spins (*15*), the phenomenon, in its manifestation for pairs of nuclear spins—the nuclear Overhauser effect (NOE) (*16*)—is widely used to determine interatomic distances in NMR studies of molecules in solution (*17, 18*).

We describe preliminary experiments that use both OP and NOEs to transfer enhanced polarization from hyperpolarized ^{129}Xe gas to solution phase without the need for radio-frequency irradiation of the spins, an effect that we denote Spin Polarization–Induced NOE (SPINOE). At first sight, the NOE enhancement from dissolved ^{129}Xe to solution spins should seem negligibly weak, because of the inefficient cross-relaxation (*19*), low Xe concentration, and the relatively short relaxation times of molecules in solution. These limitations are amply compensated, however, by the large ^{129}Xe spin polarization. We have used the SPINOE between hyperpolarized ^{129}Xe and protons in solution to monitor time-dependent MRI images and high-resolution NMR spectra of solution spins as they encounter the migrating Xe atoms.

The time dependence of the ^{129}Xe NMR signal intensity observed when hyperpolarized ^{129}Xe is dissolved in liquid benzene is shown in Fig. 1. The observed spin-lattice relaxation time of ^{129}Xe in solution, a combination of the gas and solution relaxation times, is ~200 s in normal benzene and ~1000 s in the partially deuterated sample (*20*). The difference between these two values demonstrates the influence of magnetic dipolar coupling between ^{1}H and ^{129}Xe spins on the relaxation of the ^{129}Xe magnetization; the same coupling underlies the cross-relaxation between the ^{129}Xe and ^{1}H spin systems. For the initial experiments, the partially deuterated liquids were used to promote the effects of cross-relaxation over the potentially limiting autorelaxation of the ^{1}H spins.

The effects of the dissolved hyperpolarized ^{129}Xe on the ^{1}H magnetization in liquid benzene is shown in Fig. 2. The ^{1}H NMR signal exhibits a positive or negative time-dependent NOE, depending on the sign of the ^{129}Xe magnetization, which is determined by the helicity of the laser light or the orientation of the magnetic field in the OP stage. The fractional enhancement of the ^{1}H magnetization over its thermal equilibrium value is typically observed to be ~0.1 for benzene, and between 0.5 and 2 for the partially deuterated sample. Much larger effects are anticipated in cases where Xe atoms are more effectively bound to the molecules.

On the basis of NOE theory, the following expression can be derived for the maximum change in the polarization of the solvent nuclei (**I**) due to cross-relaxation with the dissolved gas (**S**) (*21*):

$$\frac{I_z(t_0) - I_0}{I_0} = -\frac{\sigma_{IS}}{\rho_I}\frac{\gamma_S S(S+1)}{\gamma_I I(I+1)}\frac{[S_z(t_0) - S_0]}{S_0} \quad (1)$$

where γ_s and γ_I are the magnetogyric ratios of the nuclear spins, σ_{IS} is the cross-relaxation rate, and ρ_I is the autorelaxation rate of the **I** spins. The cross-relaxation rate σ_{IS} has the same value, 1.9×10^{-6} s^{-1}, for both benzene and partially deuterated benzene solutions (*22*), so the difference in the maximum enhancement of the ^{1}H polarization in these two solutions originates from the different ^{1}H relaxation rates, $\rho_I = (20\text{ s})^{-1}$ in benzene and $(160\text{ s})^{-1}$ in the partially deuterated solution. Given the spin quantum numbers and the magnetogyric ratios of the two nuclei, $I = S = ½$, $\gamma_I = 2.67 \times 10^8$ rad T^{-1} s^{-1}, and $\gamma_s = -7.44 \times 10^7$ rad T^{-1} s^{-1}, and the enhancement of the ^{129}Xe polarization at the time t_0 when the ^{1}H magnetization reaches its maximum (minimum), $S_z(t_0)/S_0 \approx 6000$, the maximum ^{1}H enhancement is estimated to be 0.06 in C_6H_6 and 0.5 in the partially deuterated solution, in general agreement with the measured values.

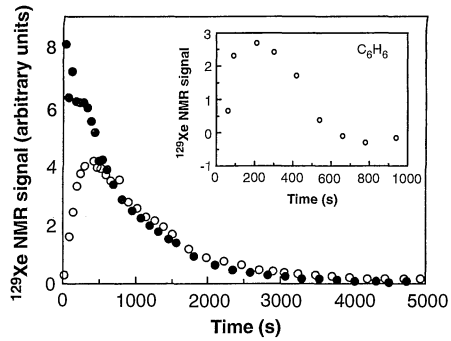

Fig. 1. Time dependence of the hyperpolarized ^{129}Xe NMR signal observed in partially deuterated benzene (25% C_6D_5H, 75% C_6D_6) and in benzene (**inset**) after exposure to hyperpolarized ^{129}Xe. (○) Xe was admitted into benzene by opening the Xe reservoir; the initial rise in signal represents the penetration of Xe into the solvent. (●) Xe was mixed with the benzene by shaking the sample after opening the reservoir, so as to produce a uniform saturated solution. ^{129}Xe spin polarization was enhanced by optical pumping with circularly polarized light at 794.7 nm. Typically, 4×10^{-4} mol of enriched ^{129}Xe (80%, EG&G Mound) were used in one experiment at a pressure of 1 atm. The difference in the ^{129}Xe signal between benzene and deuterated benzene demonstrates the effect of magnetic dipolar coupling between ^{1}H and ^{129}Xe spins on the relaxation of the ^{129}Xe. For the initial NOE experiments, the partially deuterated liquids were used in order to favor the effects of cross-relaxation over those contributing to ^{1}H autorelaxation. The apparatus for performing the optical pumping has been described previously (*31*). The sample tube, which could be closed to the atmosphere, had a small sidearm with a stopcock, allowing the isolation of the sidearm from the sample. Polarized ^{129}Xe was first frozen into the sidearm, and the whole tube was transported to the magnet. The frozen Xe was then allowed to warm up and was transferred into the sample as described above. ^{129}Xe NMR was performed at 51 MHz on a Quest 4300 spectrometer (Nalorac Cryogenics) with a home-built probe and a tipping angle of 3°.

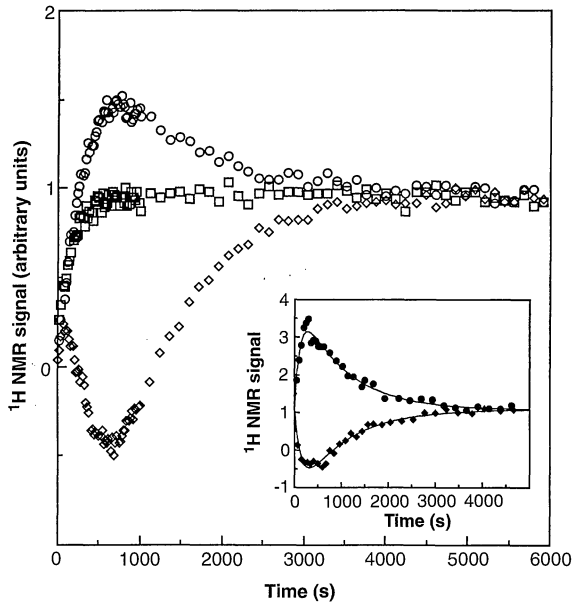

Fig. 2. Time dependence of the ^{1}H NMR signal observed after exposure of partially deuterated benzene (25% C_6D_5H, 75% C_6D_6) to hyperpolarized ^{129}Xe. The sample was exposed to Xe on the top of the NMR magnet and was then inserted into the NMR probe within a few seconds. The initial rise of the ^{1}H signal is due to spin-lattice relaxation. The ^{1}H NMR signal exhibits a positive (○) or negative (◇) NOE depending on the sign of the ^{129}Xe polarization. From the variation of the ^{1}H signal in the presence of unpolarized Xe (□), the ^{1}H T_1 relaxation time of the benzene-xenon solution is determined to be ~160 s. (**Inset**) Time dependence of the ^{1}H NMR signal after polarized ^{129}Xe was dissolved in partially deuterated benzene. Before admitting the Xe, the sample was placed in the NMR magnet for ~10 min to allow thermal equilibration of the ^{1}H magnetization. After the Xe reservoir was opened, the sample was shaken. The smooth lines represent a fit to the time-dependent solution (*29*) of Eq. 2, $I(t) = a + b(e^{-t/t_1} - e^{-t/t2})$, yielding time constants of 120 s and 1050 s (●) and 140 s and 1020 s (◆). ^{1}H NMR was performed at 185 MHz with a home-built probe and a tipping angle of 3°.

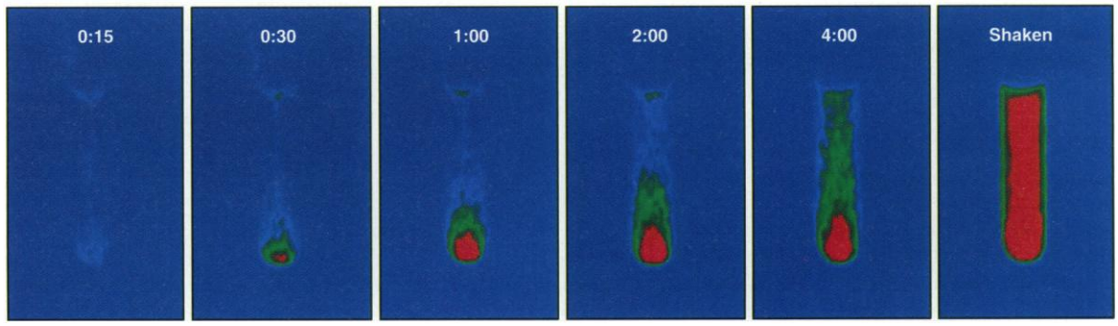

Fig. 3. Time-resolved, two-dimensional magnetic resonance images of ^{129}Xe dissolved in benzene, taken after the exposure of the benzene to hyperpolarized ^{129}Xe. A Xe concentration gradient exists immediately after the Xe is admitted, evolving with time to a more uniform solution. The 64 pixel by 128 pixel images were taken by the fast low-angle shot (FLASH) imaging method (*32*) on a Quest 4300 (Nalorac Cryogenics) spectrometer, with a tipping angle of 3° for each of the 64 signal acquisitions. The frequency-encoding gradient was 3.5 G/mm. The step size of the phase- encoding gradient pulses, which were 500 μs long, was 0.063 G/mm. The diameter of the sample tube is 7 mm, and the solution occupies a region of length 15 mm.

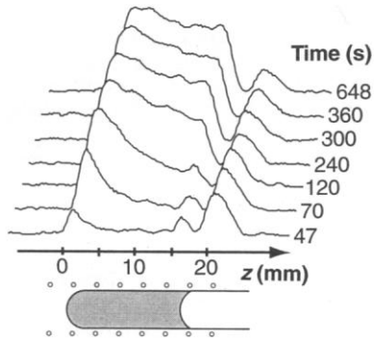

Fig. 4. Time-resolved distribution (in seconds) of ^{129}Xe magnetization in an unshaken sample of partially deuterated benzene from MRI projections along the tube axis (*z*). After 47 s three regions in the solution may be distinguished. The intensity above the solution level (above 18 mm) arises from ^{129}Xe in the gas phase, which is displaced from the dissolved ^{129}Xe signal due to its different chemical shift. The decrease of the gas signal above 21 mm along the *z* axis is due to the declining NMR sensitivity beyond the radiofrequency coil, represented by circles in the schematic diagram. The signal maximum at a position of 15.2 mm corresponds to the top of the solution, arising from Xe diffusing into the solution from the gas phase. The signal maximum at about 1.3 mm corresponds to the lower end of the tube. Thus, Xe accumulates at the bottom of the sample tube first, and a discernible Xe concentration gradient persists for up to 5 min. The concentration gradient results from natural convection due to density differences between the Xe solution and that of pure benzene, progressing ultimately to a uniform saturated Xe solution. The imaging field gradient was 2.6 G/mm.

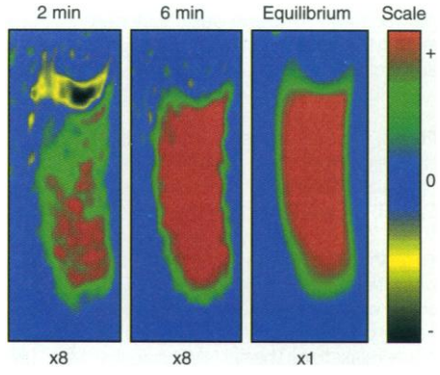

Fig. 5. Two-dimensional magnetic resonance images of the SPINOE-enhanced ^{1}H signals at 2 and 6 min after hyperpolarized ^{129}Xe was admitted to the sample tube containing normal benzene. The enhancement images were obtained by subtracting the equilibrium image shown, which is the average of four images taken after 25 min. The intensity scale in the difference images has been magnified ×8 for clarity. The maximum enhancement in the 2-min image is 0.05, that in the 6-min image, 0.12. A perceptible gradient of the enhanced ^{1}H signal is observed in the 2-min image, corresponding to the observed gradient in the Xe concentration (see Fig. 3), and the enhancement is found to be uniform in the 6-min image when the Xe concentration gradient is diminished. The negative region in the 2-min image arises from expansion of the liquid phase as Xe dissolves. The images were taken by the echo planar imaging method (*33*) in 24 ms. The frequency-encoding gradient was 3.15 G/mm; the phase-encoding gradient pulses were 0.14 G/mm and 50 μs long. The image dimension was 128 by 32 pixels, and the image was zero-filled to 256 by 256 pixels in data processing. The skew of the image is due to the inhomogeneity of the static magnetic field. The dimensions of the sample are as in Fig. 3.

The high spin-polarization and the slow relaxation of ^{129}Xe in the solvent allow for a detailed observation of the dissolution process and the flow of Xe in the solvent by means of solution MRI. Two-dimensional MRI projections along the vertical axis of the sample tube (Fig. 3) show that Xe accumulates first at the bottom of the tube, establishing a gradient in Xe concentration, and continues to dissolve into the benzene as the solution gradually becomes saturated. A detail of this process is shown in Fig. 4 where a series of the one-dimensional image intensities along the tube axis reflect the time-dependent Xe spatial distribution. The descent of Xe in the sample tube occurs because of density differences between the solution and pure benzene. The heavier Xe-rich regions of the solution, which form at the top of the solution by diffusion of the Xe into the solvent, gravitate to the lower part of the tube by natural convection, ultimately filling the tube with saturated Xe solution.

Because of the SPINOE enhancement of the ^{1}H spins proximate to the dissolved hyperpolarized ^{129}Xe, the Xe concentration gradient is expected to induce a gradient in the proton magnetization. Indeed, as shown in Fig. 5, the benzene proton magnetization images display a time-dependent gradient consistent with the spatial distribution of Xe shown in Figs. 3 and 4. It is thus possible to image indirectly the distribution and evolution of dissolved Xe by ^{1}H MRI, with the added possibility that ^{1}H chemical shifts may provide an indication of Xe distribution and partitioning, for example, among cellular components. Furthermore, differential SPINOE enhancements of ^{1}H NMR should be useful in the study of Xe-protein interactions as well as selective and enhanced nuclear Overhauser and exchange spectroscopy (NOESY) (*18*) between ^{1}H spins polarized by Xe.

Our results indicate that it is possible to image not only the hyperpolarized ^{129}Xe but also the environment in which it is accommodated, a finding that may have implications for both materials and medical applications (*11, 12, 23*), for xenon as well as for helium (*24*). Because the equilibrium polarization of the solution spins, S_0, is proportional to the magnetic field, B_0 (*21*), the relative SPINOE is inversely proportional to B_0 and is thus expected to be more pronounced at the lower magnetic fields normally used in medical imaging. Furthermore, because the NOEs depend on the proximity of the ^{129}Xe nucleus and the neighboring spins, as well as their relative motion, a large SPINOE is expected in systems where the noble gas atoms are partially immobilized in materials (*25*) or temporarily bound to molecules such as proteins (*26*), where low laboratory or rotating

frame magnetic fields may also prove advantageous (*27*). The window is thus opened to other potential applications where xenon may be adsorbed in materials and on surfaces, or dissolved in blood and other biological systems.

REFERENCES AND NOTES

1. A. Kastler, *J. Phys. Radium* **11**, 255 (1950).
2. M. A. Bouchiat, T. R. Carver, C. M. Varnum, *Phys. Rev. Lett.* **5**, 373 (1960); T. R. Carver, *Science* **141**, 599 (1963).
3. W. Happer, *Rev. Mod. Phys.* **44**, 169 (1972); W. Happer *et al.*, *Phys. Rev. A* **29**, 3092 (1984); B. Driehuys, G. D. Cates, W. Happer, *Phys. Rev. Lett.* **74**, 4943 (1995).
4. M. A. Springuelhuet, J. L. Bonardet, J. Fraissard, *Appl. Magn. Reson.* **8**, 427 (1995); M. Pfeffer and O. Lutz, *J. Magn. Reson.* **A108**, 106 (1994).
5. D. Raftery *et al.*, *Phys. Rev. Lett.* **66**, 584 (1991).
6. B. Driehuys *et al.*, *Phys. Lett.* **A184**, 88 (1993).
7. C. R. Bowers, H. W. Long, T. Pietrass, H. C. Gaede, A. Pines, *Chem. Phys. Lett.* **205**, 168 (1993).
8. H. W. Long *et al.*, *J. Am. Chem. Soc.* **115**, 8491 (1993).
9. K. F. Woodman, P. W. Frank, M. D. Richards, *J. Navig.* **40**, 366 (1987).
10. M. Mehring, S. Appelt, H. Langen, G. Waeckerle, in *High Precision Navigation 91*, K. Linkwitz and U. Hangleiter, Eds. (Duemmler Verlag, Bonn, 1992), pp. 559–568.
11. M. S. Albert *et al.*, *Nature* **370**, 199 (1994).
12. Y.-Q. Song *et al.*, *J. Magn. Reson.* **A115**, 127 (1995).
13. A. W. Overhauser, *Phys. Rev.* **91**, 476 (1953); *ibid.* **92**, 411 (1953).
14. T. R. Carver and C. P. Slichter, *ibid.* **92**, 212 (1953); C. P. Slichter, *ibid.* **102**, 975 (1956).
15. Reviewed by K. H. Hausser and D. Stehlik [*Adv. Magn. Reson.* **3**, 79 (1968)].
16. I. Solomon, *Phys. Rev.* **99**, 559 (1955).
17. A. G. Redfield, *IBM J. Res. Dev.* **1**, 1 (1957).
18. A. Kumar, R. R. Ernst, K. Wuthrich, *Biochem. Biophys. Res. Commun.* **95**, 1 (1980).
19. K. Bartik, M. Luhmer, J. Reisse, paper presented at the 35th Experimental Nuclear Magnetic Resonance Conference, Pacific Grove, CA, 1994; Y. Xu, P. Tang, paper presented at the society of Magnetic Resonance Annual Meeting, Nice, France, 19 to 25 August 1995.
20. A. Moschos and J. Reisse, *J. Magn. Reson.* **95**, 603 (1991); P. Diehl and J. Jokisaari, *ibid.* **88**, 660 (1990). Our value for the spin-lattice relaxation time for ^{129}Xe in partially deuterated benzene is longer than the value given in these references for fully deuterated benzene, probably because of Xe exchange between gas and solution phases.
21. Cross-relaxation between the two spin systems, **I** and **S**, is described by the Solomon equations (*28, 29*):

$$\frac{d}{dt} I_z = -\rho_I(I_z - I_0) - \sigma_{IS}(S_z - S_0)$$
$$\frac{d}{dt} S_z = -\rho_S(S_z - S_0) - \sigma_{SI}(I_z - I_0) \quad (2)$$

where I_z and S_z are the z components of the **I** and **S** spins and I_0 and S_0 are the equilibrium values; ρ_I and ρ_S are the autorelaxation rates. The cross-relaxation rates, σ_{IS} and σ_{SI}, are related to each other by

$$\sigma_{IS} = \frac{I(I+1)N_S}{S(S+1)N_I}\sigma_{SI} \quad (3)$$

where N_I and N_S are the concentrations of **I** and **S** spins in the liquid. At time t_0, I_z goes through either a minimum or a maximum, depending on the sign of $[S_z(t_0) - S_0]$. At this time, $\frac{d}{dt} I_z = 0$, and from Eq. 2 one obtains

$$\frac{I_z(t_0) - I_0}{I_0} = -\frac{\sigma_{IS}}{\rho_I}\frac{\gamma_S S(S+1)}{\gamma_I I(I+1)}\frac{[S_z(t_0) - S_0]}{S_0} \quad (4)$$

where the high temperature approximation for S_0 and I_0 was used, $I_0 \approx I(I+1)\hbar\gamma_I B_0/(3k_B T)$, $S_0 \approx S(S+1)\hbar\gamma_S B_0/(3k_B T)$, where $\hbar$ is the Planck constant, k_B the Boltzmann constant, B_0 the external magnetic field strength, and T the temperature of the liquid. σ_{IS} can be estimated by means of Eq. 3 and the relation between σ_{SI} and ρ_S^{SI}, the part of the autorelaxation rate of spins **S** due to their dipolar interaction with spins **I**. In the fast motion limit,

$$\sigma_{SI} = \frac{S(S+1)}{2I(I+1)}\rho_S^{SI} \quad (5)$$

From Eqs. 3 and 5 one then obtains

$$\sigma_{IS} = \frac{N_S}{2N_I}\rho_S^{SI} \quad (6)$$

22. In order to estimate the cross-relaxation rate σ_{IS} (Eq. 6), we use $\rho_S^{SI} = (390\ s)^{-1}$, determined from the value of the spin-lattice relaxation times (T_1) of ^{129}Xe in benzene and fully deuterated benzene solution (*20*). The ratio of ^{129}Xe (80% enriched) to ^1H in C_6H_6 is $N_S/N_I = 0.0015$, using the solubility data of Xe in benzene (0.011 mole fraction at 1 atm and 25°C) (*30*). One obtains $\sigma_{IS} = 1.9 \times 10^{-6}\ s^{-1}$, independent of the concentration of **I** spins (*29*) and assumed to be the same in the partially deuterated benzene.
23. Early gas MNR images of a lung were obtained by Heidelberger and Lauterbur, Society of Magnetic Resonance in Medicine, 1st annual general meeting, 1982).
24. H. Middleton, R. D. Black, B. Saam, G. D. Cates, W. Happer, *Magn. Reson. Med.* **33**, 271 (1995).
25. J. B. Miller, J. H. Walton, C. M. Roland, *Macromolecules* **26**, 5602 (1993).
26. R. F. Tilton and J. I. D. Kuntz, *Biochemistry* **21**, 6850 (1982).
27. A. G. Redfield, *Phys. Rev.* **98**, 1787 (1955); S. R. Arepalli, C. P. J. Glaudemans, J. G. Doyle Daves, P. Kovac, A. Bax, *J. Magn. Reson. B* **106**, 195 (1995).
28. A. Abragam, *Principles of Nuclear Magnetism* (Clarendon, Oxford, 1961).
29. J. H. Noggle and R. E. Schirmer, *The Nuclear Overhauser Effect: Chemical Applications* (Academic Press, New York, 1971).
30. W. F. Linke and A. Seidell, *Solubilities* (Van Nostrand, Princeton, NJ, ed. 4, 1958).
31. H. C. Gaede, thesis, University of California at Berkeley (1995); H. C. Gaede *et al.*, *Appl. Magn. Reson.* **8**, 373 (1995).
32. A. Haase, J. Frahm, D. Matthaei, W. Hanicke, K. D. Merboldt, *J. Magn. Reson.* **67**, 258 (1986).
33. P. Mansfield, *J. Phys. C* **10**, L55 (1977).

34. Supported by the Director, Office of Energy Research, Office of Basic Energy Sciences, Materials Sciences Division, of the U.S. Department of Energy under contract DE-AC03-76SF00098. Y.-Q.S. was a Miller Research Fellow, partially supported by the Miller Institute for Basic Research in Science; S.A. was partially supported by the Deutsche Forschungsgemeinschaft; and T. R. was partially supported by the National Science Foundation through grant FD93-11913 administered by the Department of Physics.

7 November 1995; accepted 24 January 1996

Caste-Selective Pheromone Biosynthesis in Honeybees

Erika Plettner, Keith N. Slessor,* Mark L. Winston, James E. Oliver

Queen and worker honeybees (*Apis mellifera* L.) produce a caste-related blend of functionalized 8- and 10-carbon fatty acids in their mandibular glands. The biological functions of these compounds match the queen's reproductive and the worker's nonreproductive roles in the colony. Studies with deuterated substrates revealed that the biosynthesis of these acids begins with stearic acid, which is hydroxylated at the 17th or 18th position. The 18-carbon hydroxy acid chains are shortened, and the resulting 10-carbon hydroxy acids are oxidized in a caste-selective manner, thereby determining many of the functional differences between queens and workers.

One of the most remarkable aspects of social insect biology is the separation of female colony members into reproductive and nonreproductive castes: queens and workers (*1*). A major difference between the female honeybee castes is the blend of 8- and 10-carbon functionalized fatty acids found in the mandibular glands. Queens have predominantly 9-hydroxy-(*E*)2-decenoic acid (9-HDA) and other acids functionalized at the penultimate ($\omega - 1$) position, among them 9-keto-(*E*)2-decenoic acid (ODA) (*2*). Workers have acids functionalized at the last (ω) position such as 10-hydroxy-(*E*)2-decenoic acid (10-HDA), its saturated counterpart, and the corresponding diacids (*3*). The queen's acids, 9-HDA and ODA, are components of the queen mandibular pheromone (QMP), a powerful attractant of workers and one cue responsible for the retinue of workers around the queen. The queen asserts her reproductive dominance by mediating some worker activities associated with colony growth and reproduction through her QMP signal (*2, 4, 5*). The worker-produced acids are secreted in brood food (*6*) where they may function as preservatives (*7*) and larval nutrients (*8*). Thus, queens and workers produce compounds that fit their respective reproductive and nonreproductive roles and differ only in the position of the functional group. Here, we report the elucidation of the biochemical pathway that determines whether a honeybee female will produce

E. Plettner and K. N. Slessor, Department of Chemistry, Simon Fraser University, Burnaby, British Columbia V5A 1S6, Canada.
M. L. Winston, Department of Biological Sciences, Simon Fraser University, Burnaby, British Columbia V5A 1S6, Canada.
J. E. Oliver, U.S. Department of Agriculture, Agricultural Research Service, Beltsville Agriculture Research Center, Beltsville, MD 20705–2350, USA.

*To whom correspondence should be addressed.